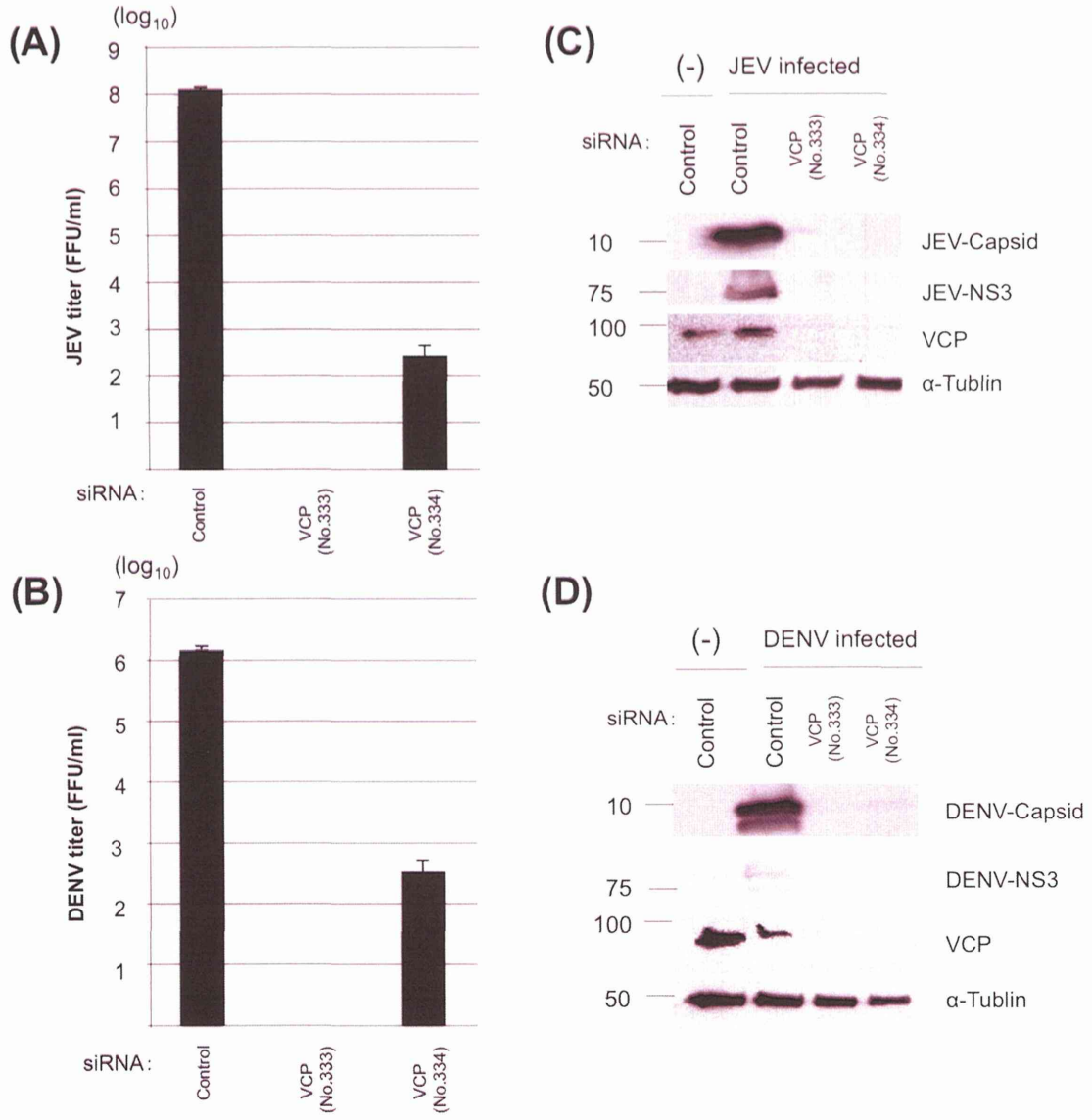

Fig7 VCPのノックダウンによるJEV及びDENV増殖への影響

(A) VCPノックダウン細胞でのJEVの増殖。VCP siRNA (lane 2-3)又はコントロールsiRNA(lane1)をトランスフェクションした細胞にJEVをMOI=0.3で感染させ、3日後の培養上清に含まれる感染性JEVをフォーカスフォーミングアッセイによって測定した。 (B) VCPノックダウン細胞でのDENVの増殖。VCP siRNA (lane 2-3)又はコントロールsiRNA(lane1)をトランスフェクションした細胞にDENVをMOI=0.3で感染させ、3日後の培養上清に含まれる感染性DENVVをフォーカスフォーミングアッセイによって測定した。 (C) VCPノックダウン細胞でのJEV蛋白質の発現。(A)の実験で用いた細胞を溶解し、ウェスタンブロットによってJEV-Capsid(low1)、JEV-NS3(low2)、VCP(low3)、α-tubulin(low4)をそれぞれの蛋白質を認識する特異的な抗体を用いて検出した。 (D)VCPノックダウン細胞でのDENV蛋白質の発現。(B)の実験で用いた細胞を溶解し、ウェスタンブロットによってDENV-Capsid(low1)、DENV-NS3(low2)、VCP(low3)、α-tubulin(low4)をそれぞれ検出した。

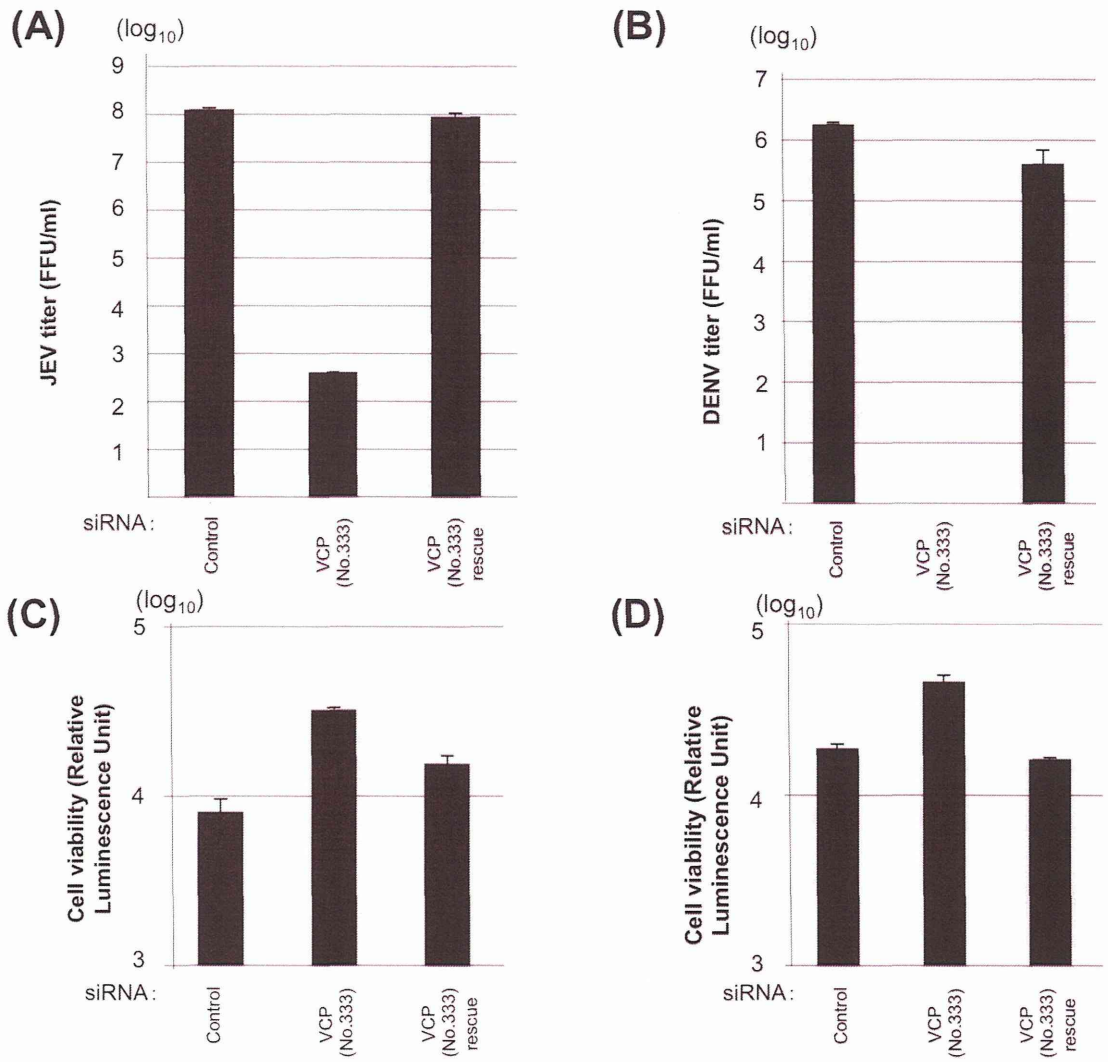

Fig8 siRNAに認識されない核酸配列をもつVCPの発現による機能回復

(A)VCPノックダウンのJEV増殖に与える影響。VCPに対するsiRNA(lane2-3)又はコントロールsiRNA(lane1)のトランスフェクションと同時に、siRNAに認識されない核酸配列をもつVCP発現プラスミド(lane3)、またはエンプティープラスミド(lane2)をトランスフェクションし、VCPノックダウンによる影響が打ち消されるかどうか調べた。siRNA/プラスミドDNA混合液をトランスフェクション後、JEVを感染させ、3日後に上清中に含まれる感染性ウイルス粒子数をフォーカスフォーミングアッセイにて測定した。(B) VCPノックダウンのDENV増殖に与える影響。VCPに対するsiRNA(lane2-3)又はコントロールsiRNA(lane1)のトランスフェクションと同時に、siRNAに認識されない核酸配列をもつVCP発現プラスミド(lane3)、またはエンプティープラスミド(lane2)をトランスフェクションし、DENVを感染させ、3日後に上清中に含まれる感染性ウイルス粒子数をフォーカスフォーミングアッセイにて測定した。(C&D)VCPノックダウン細胞の生存率。(A)または(B)の実験で用いた細胞の生存率をCellTiter-Gloアッセイによって測定した。

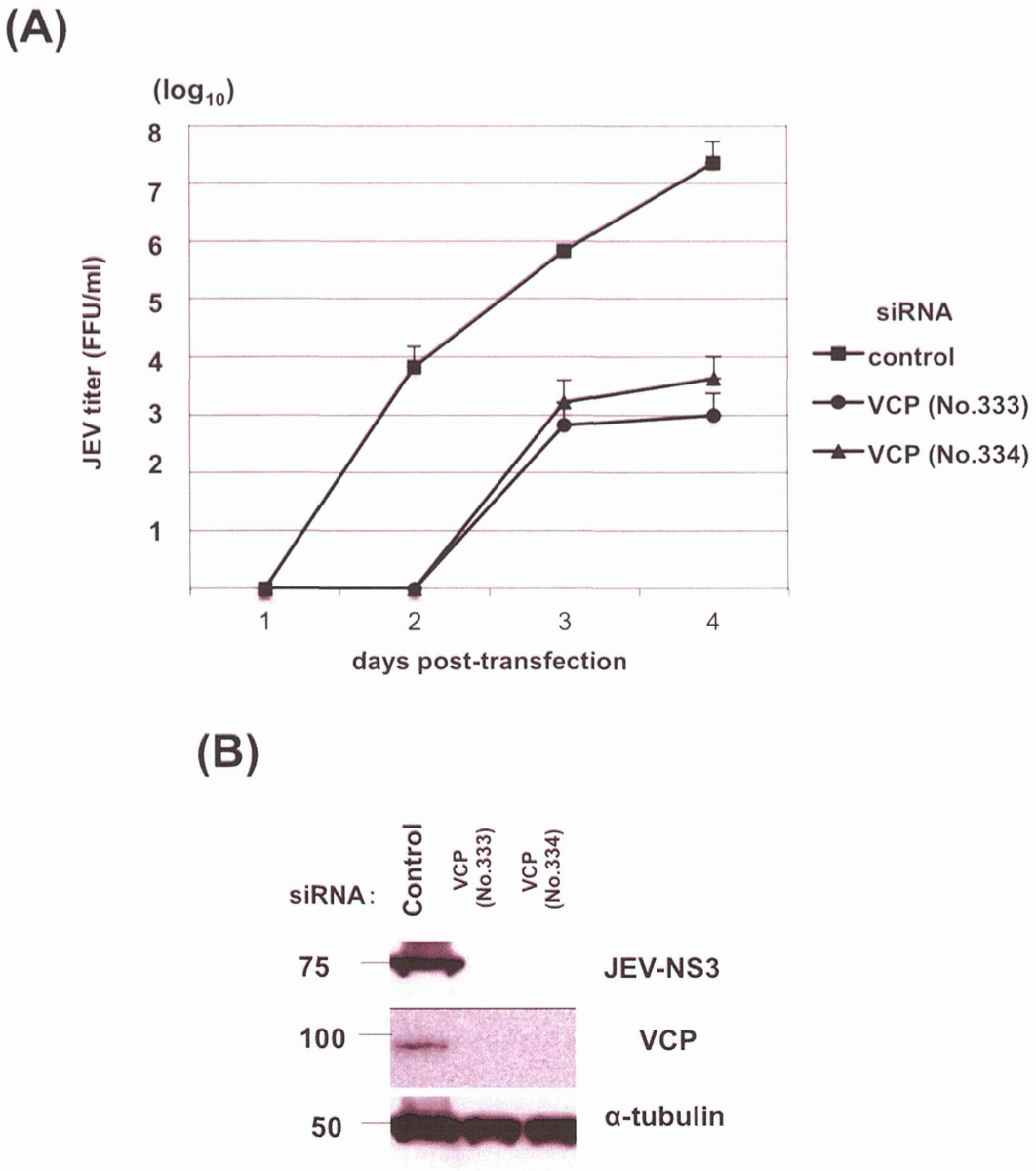

Fig.9 JEVゲノムRNAトランスフェクションによるウイルス産生系におけるVCPノックダウンの影響

(A)ウイルス産生量の変化。VCPノックダウン細胞(●、▲)、又はコントロールsiRNAをトランスフェクションした細胞(■)に、*in vitro*で合成したJEVのゲノムRNAをトランスフェクションし、経時毎培養上清中に含まれる感染性ウイルス量をフォーカスフォーミングアッセイにて測定した。(B)　ウイルス蛋白量の測定。(A)の実験で用いた感染後96時間後の細胞(VCP siRNA: lane2-3, control siRNA: lane1) を溶解し、ウェスタンブロット法によりJEV-NS3(top panel)、VCP(middle panel)又はα-tubulin(bottom panel)をそれぞれの因子に対する特異的抗体を用いて検出した。

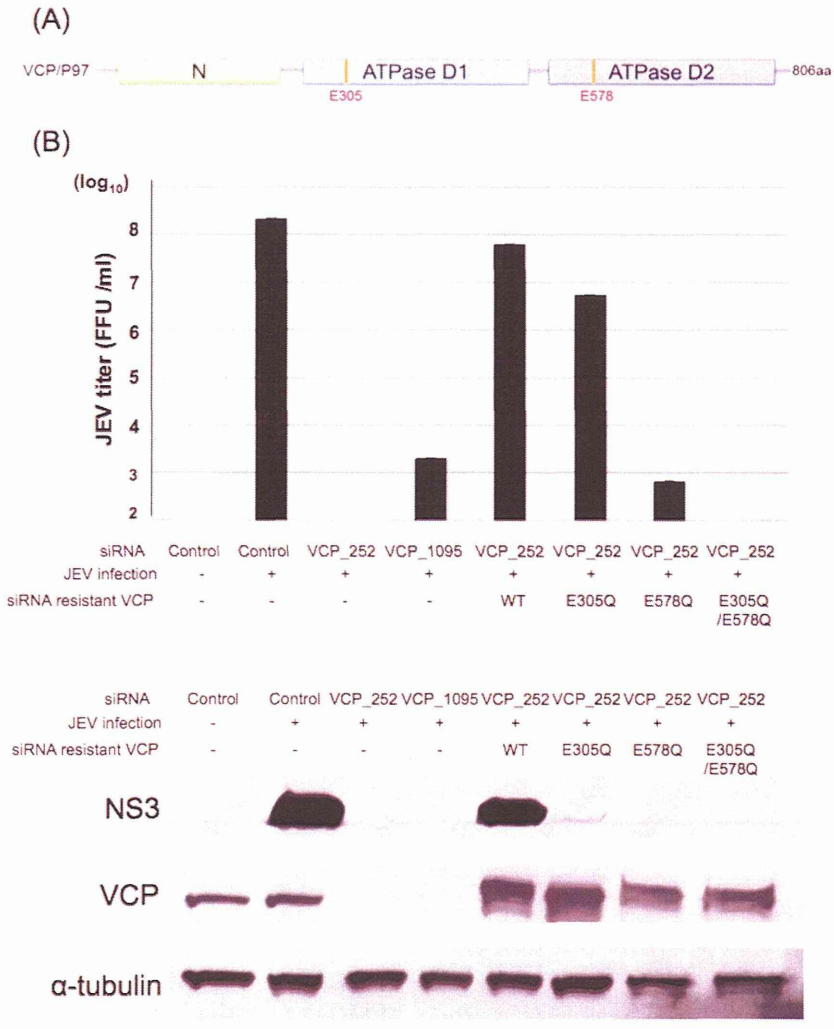

Fig.10 VCP の ATPase 不活性化変異体がウイルス増殖に与える影響。
VCP の一次構造と、本実験で使用した ATPase 変異体の変異導入位置を示した模式図。2 つの ATPase ドメインを不活性化させるために、305 番目、または 578 番目のグルタミン酸をそれぞれアラニンに置換した変異体と、両方同時に置換した二重変異体を作製した。(B) 野生型 VCP と ATPase 不活性化変異体の JEV 増殖に与える効果。siRNA VCP_252 に対して抵抗性を示すサイレンス変異を導入した野生型 VCP と ATPase 変異体を、siRNA と同時にトランスフェクションした。その後 JEV を感染させ、72 時間後の上清中に含まれる感染性ウイルス量をフォーカスフォーミングアッセイにて測定した。また、ウエスタンブロット法により細胞中に含まれる NS3、VCP、α-tubulin をそれぞれを特異的に認識する抗体を用いて検出した。

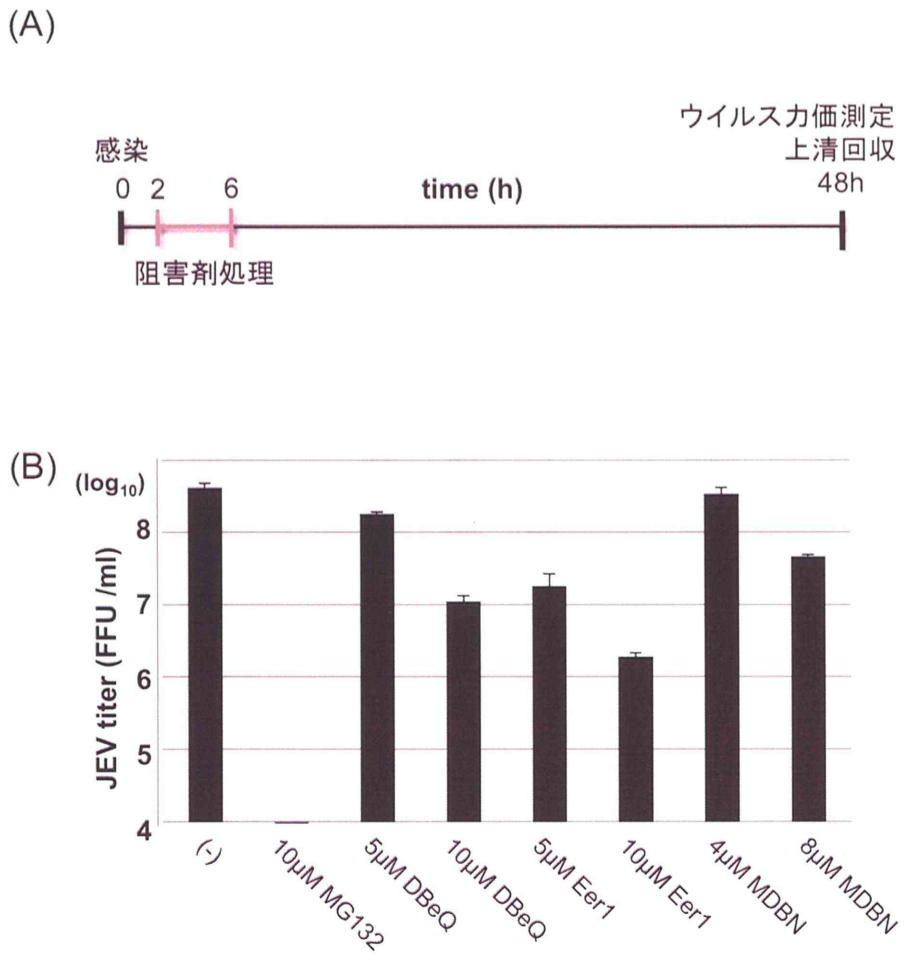

Fig.11 VCP 阻害剤処理が JEV 増殖に与える影響。
(A) 本実験のタイムコースの概略図。JEV の感染時を 0 時間とした。培養細胞にウイルス液を添加後 2 時間吸着させた後、5μM または 10μM の MG132、DBeQ、EerI、MDBN を 4 時間処理した。その後、阻害剤の含まない培地に交換した後 48 時間培養し、上清中に含まれるウイルス量をフォーカスフォーミングアッセイによって測定した。(B) 各種低分子化合物添加によるウイルス増殖能の変化。縦軸はウイルス感染価を示す。

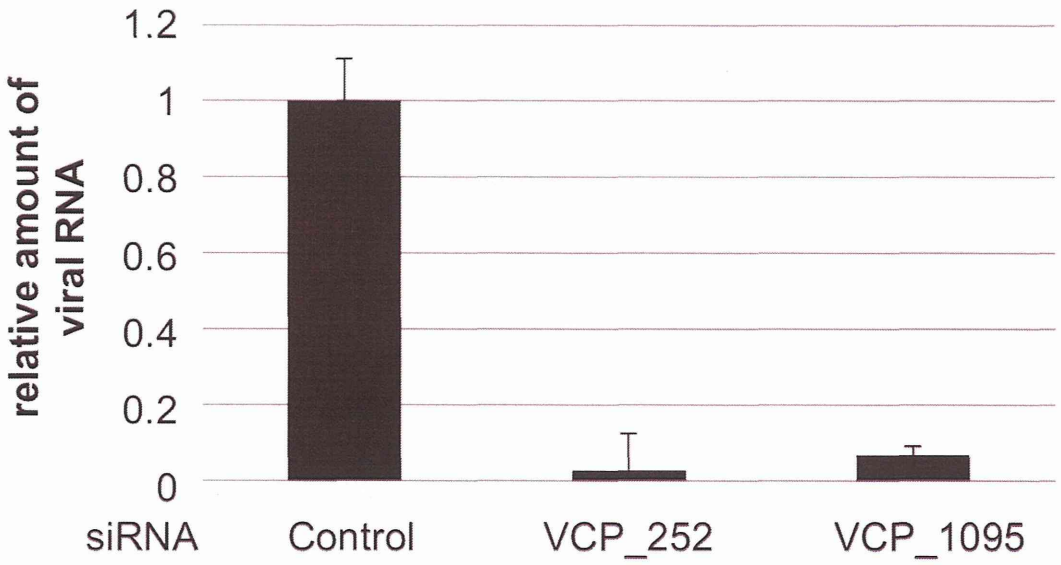

Fig.12 VCP ノックダウンによるウイルスゲノム複製に与える影響。
コントロール siRNA もしくは、VCP siRNA をトランスフェクションした細胞に、m.o.i=0.3 にて JEV を感染させた。感染 72 時間後の細胞を回収し、細胞内に存在するウイルスゲノム RNA 量を qRT-PCR を用いて測定した。各サンプルの RNA 量を β-actin の RNA 量で補正し、コントロールの値を 1 としたときの相対値を示した。

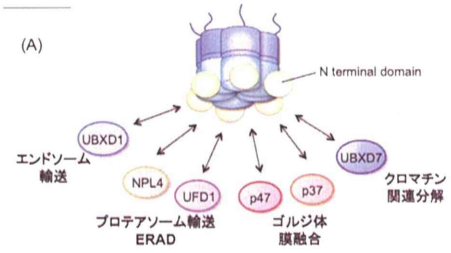
(A)
N terminal domain
UBXD1
エンドソーム
輸送
NPL4
UFD1
p47
p37
UBXD7
クロマチン
関連分解
プロテアソーム輸送
ERAD
ゴルジ体
膜融合

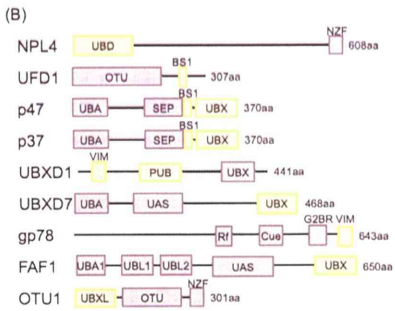
(B)
NPL4 UBD NZF 608aa
UFD1 OTU BS1 307aa
p47 UBA SEP BS1 UBX 370aa
p37 UBA SEP BS1 UBX 370aa
UBXD1 VIM PUB UBX 441aa
UBXD7 UBA UAS UBX 468aa
gp78 RF Cue G2BR VIM 643aa
FAF1 UBA1 UBL1 UBL2 UAS UBX 650aa
OTU1 UBXL OTU NZF 301aa

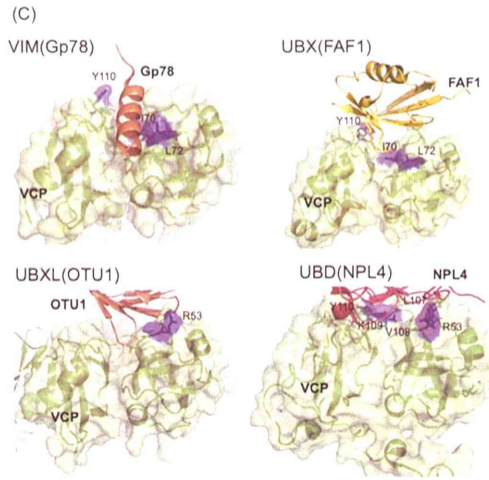
(C)
VIM(Gp78)
Y110
Gp78
I70
L72
VCP
UBX(FAF1)
FAF1
UBXL(OTU1)
OTU1
R53
UBD(NPL4)
NPL4
L109
K109
V108

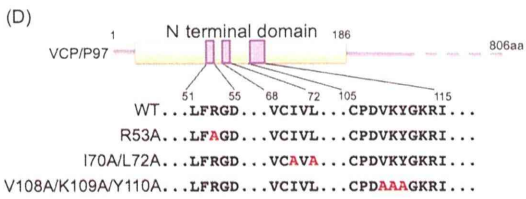
(D)
N terminal domain
VCP/P97
1
186
806aa
51
55
68
72
105
115
WT...LFRGD...VCIVL...CPDVKYGKRI...
R53A...LFAGD...VCIVL...CPDVKYGKRI...
I70A/L72A...LFRGD...VCAVA...CPDVKYGKRI...
V108A/K109A/Y110A...LFRGD...VCIVL...CPDAAAGKRI...

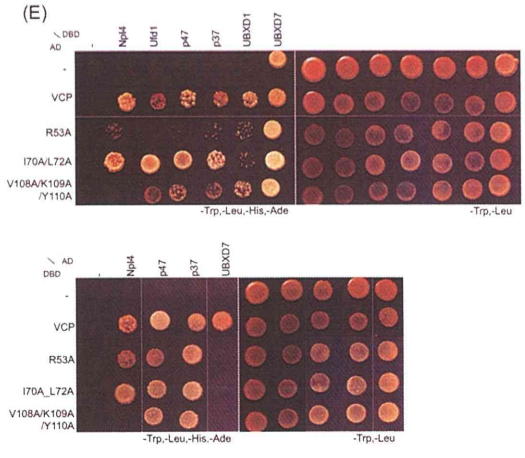
(E)
DBD
AD
Npl4
Ufd1
p47
p37
UBXD1
UBXD7
VCP
R53A
I70A/L72A
V108A/K109A
/Y110A
-Trp,-Leu,-His,-Ade
-Trp,-Leu

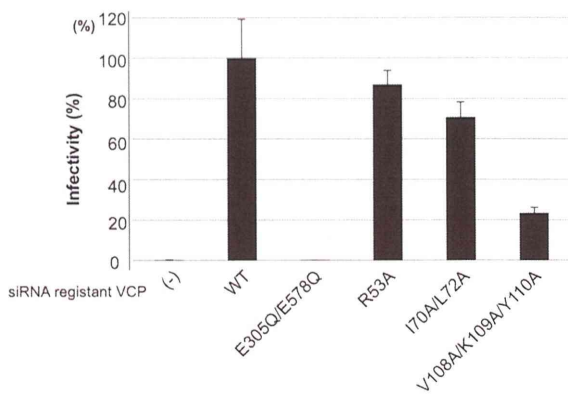
(F)
Infectivity (%)
(%)
120
100
80
60
40
20
0
siRNA registant VCP
(-)
WT
E305Q/E578Q
R53A
I70A/L72A
V108A/K109A/Y110A

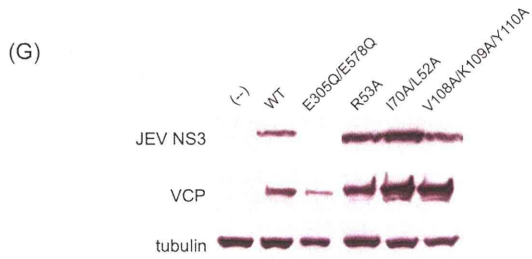
(G)
(-)
WT
E305Q/E578Q
R53A
I70A/L52A
V108A/K109A/Y110A
JEV NS3
VCP
tubulin

Fig.13 VCP コファクターがフラビウイルス増殖に与える影響。
(A)コファクターの種類を変えることで、様々な細胞内イベントに対応する。 (B) 代表的な VCP コファクタの一次構造。コファクタに存在する様々なドメインのうち、VCP 結合ドメインを黄色で示した。(C) VCP ND と、VCP ND に結合するドメインの結晶構造。VCP ND（緑）と gp78-VIM（黄土色、PDB ID:3TIW）、FAF1-UBX（黄色、PDB ID:3QQ8）、OTU1-UBXL（肌色、PDB ID:4KDI）、NPL4-UBD（桃色、PDB ID:2PJH）を示した。コファクタとの結合に重要であると予測されるアミノ酸残基を青色で示した。(D) 本実験で作製した VCP ND 変異体の模式図。(E) 酵母ツーハイブリッド法による VCP コファクターと VCP ND 変異体の結合。野生型 VCP または変異体 VCP を発現するベクターと、各種 VCP コファクターを発現するベクターを酵母に形質転換し、-Leu, -Trp（コントロール培地）及び-Leu, -Trp, -Ade, -His （選別培地） の２種類の SD 培地に播種し、7 日間培養した。(F) VCP ND 変異体のウイルス増殖における機能解析。各種 VCP ND 変異体に VCP_252 siRNA に抵抗性を持つようにサイレンス変異を導入し、VCP siRNA と共に HEK293A にトランスフェクションした。その後、m.o.i=0.3 の JEV を感染させ、72 時間後の上清中に含まれる感染性ウイルス粒子をフォーカスフォーミングアッセイにて計測した。野生型 VCP を入れ戻した時のウイルス感染力価を 100%としたときのウイルス感染力価をグラフに示した。(G) (F)の実験で用いた細胞中に含まれる VCP、α-Tubulin、JEV NS3 量をウエスタンブロット法によりそれぞれを特異的に認識する抗体を用いて検出した。

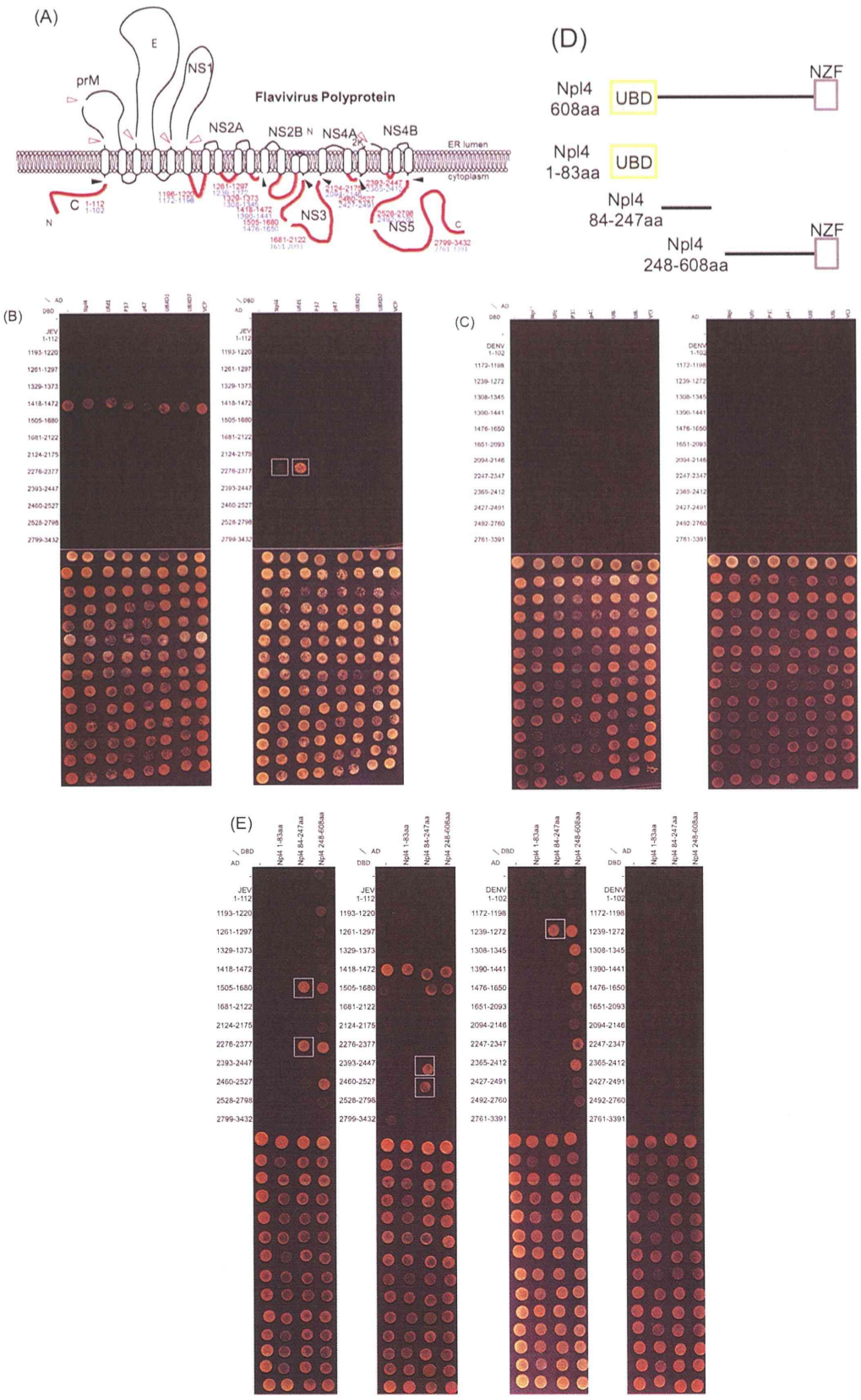
(A)
E
prM
NS1
Flavivirus Polyprotein
NS2A
NS2B
NS4A
NS4B
ER lumen
cytoplasm
C 1-112
1-102
N
NS3
NS5
C
(D)
Npl4
608aa
UBD
NZF
Npl4
1-83aa
UBD
Npl4
84-247aa
Npl4
248-608aa
NZF
(B)
(C)
(E)
JEV
1-112
DENV
1-102
Npl4 1-83aa
Npl4 84-247aa
Npl4 248-608aa

Fig.14　VCP または VCP コファクターと結合するウイルス非構造タンパク質の検索。
(A) フラビウイルスポリプロテインの膜貫通領域を示した一次構造と、酵母ツーハイブリッド法で用いた細胞質側に露呈するペプチド領域を示した模式図。黒矢印は NS3 タンパク質、白矢印は宿主因子による切断箇所を示した。酵母ツーハイブリッドベクターに組み込んだ領域を赤い線で示した。JEV（青字）または DENV（赤字）のアミノ酸配列番号をそれぞれ示す。(B) 酵母ツーハイブリッド法による JEV NS タンパク質と VCP コファクターとの結合の探索。(A)で示した JEV 及び DENV の細胞質領域のペプチドと、VCP 及び 6 種類の VCP コファクターを発現する酵母ツーハイブリッドベクターを酵母に形質転換し-Leu, -Trp （コントロール培地）及び-Leu, -Trp, -Ade, -His （選別培地） の SD 培地に播種し、3 日間培養した。(C) 酵母ツーハイブリッド法による DENV NS タンパク質と VCP コファクターとの結合の探索。 (D) NPL4 の末端欠損変異体の一次構造を示した模式図。(E) 酵母ツーハイブリッド法による NPL4 末端欠損変異体とフラビウイルスタンパク質の結合。陽性のシグナルを白四角で示す。

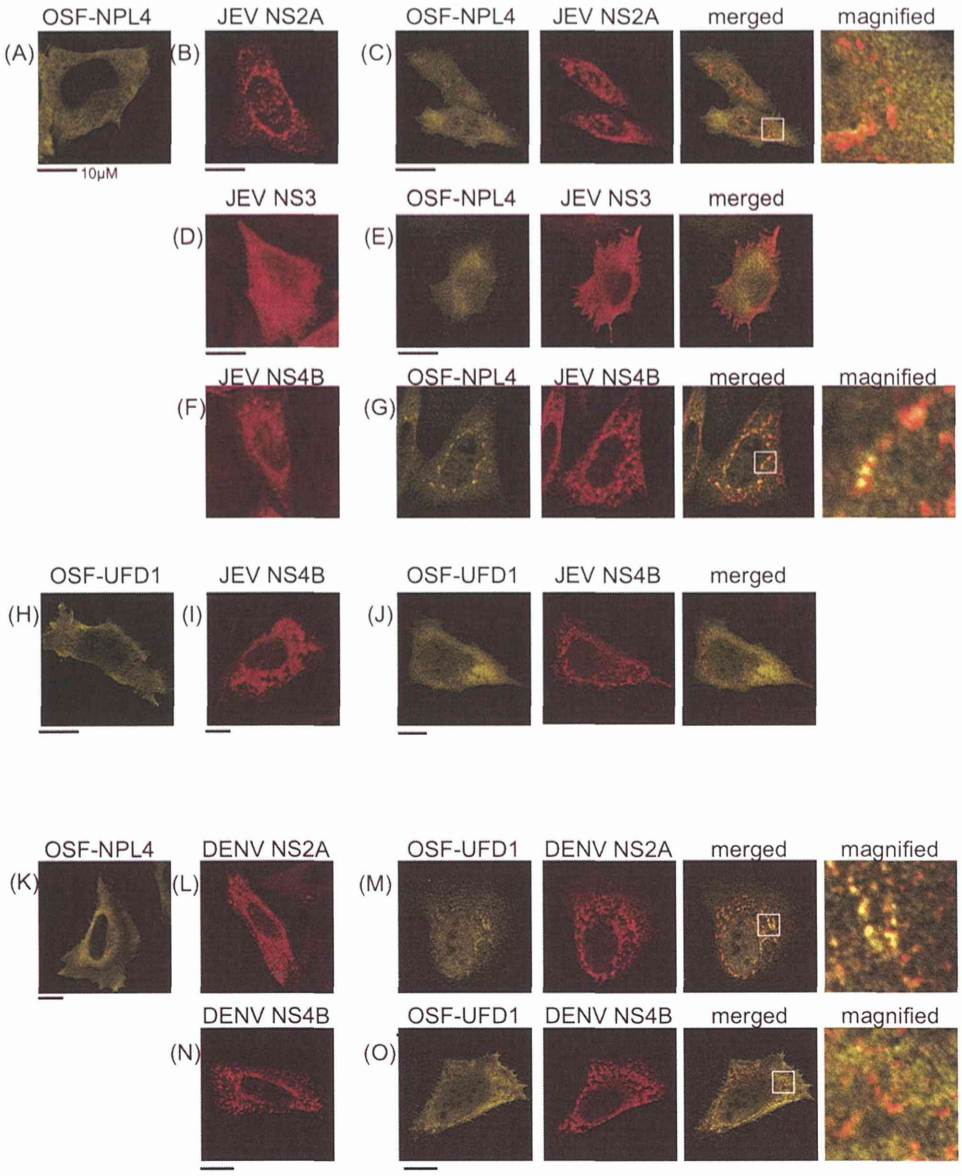

Fig.15 VCP コファクターとウイルス非構造タンパク質の局在。
OSF タグを付加したコファクターと、myc タグを付加したウイルスタンパク質を発現するベクターを HeLa 細胞にトランスフェクションし、24 時間後に 4%PFA で固定し、FLAG 抗体と myc 抗体を用いて VCP コファクターとウイルスタンパク質を検出した。(A) OSF-NPL4 を単独で発現させた細胞、(B) JEV NS2A-myc を単独で発現させた細胞、(C) OSF-NPL4 と JEV NS2A-myc を共発現させた細胞、(D) myc-JEV NS3 と NS2B を発現させた細胞、(E) OSF-NPL4 と myc-JEV NS3 及び NS2B を共発現させた細胞、(F) JEV NS4B-myc を単独で発現させた細胞、(G) OSF-NPL4 と JEV NS4B-myc を共発現させた細胞、(H) OSF-UFD1 を単独で発現させた細胞、(I) JEV NS4B-myc を単独で発現させた細胞、 (J) OSF-UFD1 と JEV NS4B-myc を共発現させた細胞、(K) OSF-NPL4 を単独で発現させた細胞、(L) DENV NS2A-myc を単独で発現させた細胞、(M) OSF-NPL4 と DENV NS2A-myc を共発現させた細胞、(N) DENV NS4B-myc を単独で発現させた細胞、(M) OSF-NPL4 と DENV NS4B-myc を共発現させた細胞をっ固定し、それぞれの細胞内に発現する因子を抗 FLAG 抗体（緑）、抗 myc 抗体（赤）を用いて検出した。右側に画像に融合させた画像（merged）と拡大させた画像（magnified）を示す。

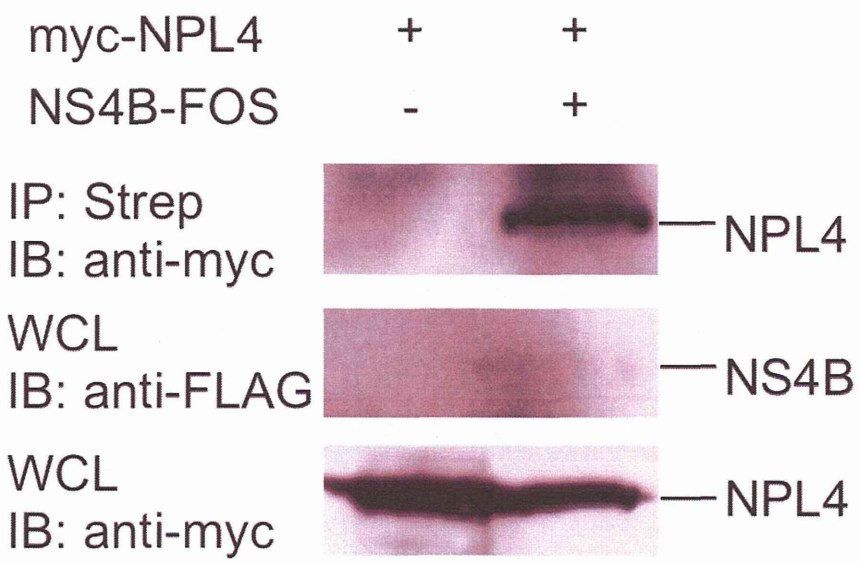

Fig.16 免疫沈降法による JEV NS4B と NPL4 の結合。
OSF タグを付加した NS4B と myc タグを付加した NPL4 を HEK293A 細胞にトランスフェクションし、共発現させた。48 時間後に細胞を溶解し、Strep-tactin ビーズを用いて、OSF-NS4B を精製した。精製したサンプルを SDS-PAGE にて展開後、ウエスタンブロット法により、NS4B と共精製された NPL4 を抗 myc タグ抗体を用いて検出した(パネル 1)。細胞溶解液に含まれる JEV NS4B(パネル 2)と NPL4(パネル 3)につても抗 FLAG タグ抗体及び抗 myc タグ抗体を用いて検出した。

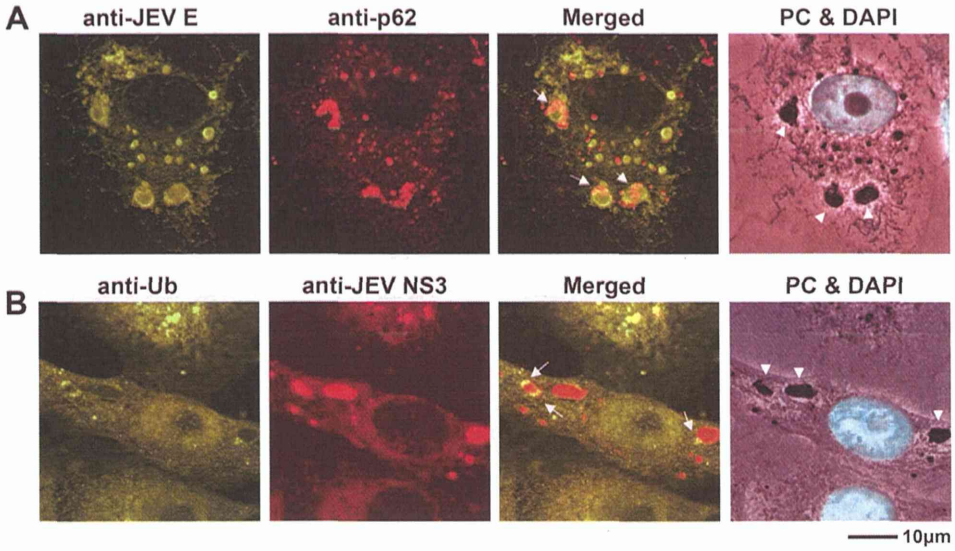

Fig. 17 p62 とユビキチンがウイルス複製オルガネラにリクルートされる
Vero cells are infected JEV at M.O.I=1.0, fix at 48h postinfection, stained with anti-JEV E mouse monoclonal and anti-p62 rabbit polyclonal antibodies (A) or anti-ubiquitin (FK2) mouse monoclonal and anti-JEV NS3 rabbit polyclonal antibodies (B), and detected mouse or rabbit primary antibodies by AlexaFluoro488 conjugated anti-mouse IgG (lane1, green) and AlexaFluoro594 conjugated anti-rabbit IgG (lane2, red). Merged images of green and red (lane 3), and phase contrast (gray) and DNA staining (blue) (lane4) were shown respectively. Bar indicates 10μm.

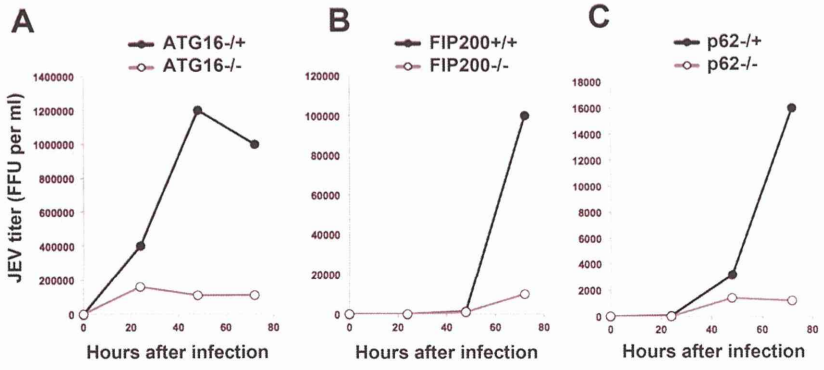

Fig18. ATG 因子群と p62 はフラビウイルスの増殖に必要である。
ATG16L1 (A), FIP200 (B), or p62(C) knockout MEF cells were infected with JEV at M.O.I=0.3. Culture supernatants are harvested at indicated time after infection, and viral infectious titers are measured by performing focus -forming assay. WT MEFs derived from same littermates are used as control cells.

II. 研究成果の刊行に関する一覧表

雑誌

発表者氏名	論文タイトル名	発表誌名	巻号	ページ	出版年
Suzuki, H., Tabata, K., **Morita, E.**, Kawasaki, M., Kato, R., Dobson, RJ., Yoshimori, T.,	Structural basis of the autophagy-related LC3/Atg13 LIR complex: recognition and interaction mechanism.	***Structure.***	22(1)	1-12	2014
Fujita, N.†, Morita, E. †, Itoh, T., Tanaka, A., Nakaoka, M., Osada, Y., Umemoto, T., Saitoh, T., Nakatogawa, H., Kobayashi, S., Haraguchi, T., Guan, J.L., Iwai, K., Tokunaga, F., Saito, K., Ishibashi, K., Akira, S., Fukuda, M., Noda, T.,	Recruitment of the autophagic machinery to endosomes during infection is mediated by ubiquitin	***J Cell Biol.***	203(1)	115-128	2013
Tripathi, L.P., Kambara, H., Chen, Y.A., Nishimura, Y., Moriishi, K., Okamoto, T., Morita, E., Abe, T., Mori, Y., Matsuura, Y., Mizuguchi, K.	Understanding the biological context of NS5A-host interactions in HCV infection: a network-based approach	***J Proteome Res.***	12(6)	2537-2551	2013
Katoh H, Okamoto T, Fukuhara T, Kambara H, **Morita E,** Mori Y, Kamitani W, Matsuura Y.	Japanese Encephalitis Virus Core Protein Inhibits Stress Granule Formation through an Interaction with Caprin-1 and Facilitates Viral Propagation.	***J Virol.***	87(1)	489-502	2013

発表者氏名	論文タイトル名	発表誌名	巻号	ページ	出版年
Morita, E., Arii J, Christensen D, Votteler J, Sundquist WI.	Attenuated protein expression vectors for use in siRNA rescue experiments.	***Biotechniques.***	0	1-5	2012
Tripathi, L.P., Kambara, H., Moriishi, K., **Morita, E.**, Abe, T., Mori, Y., Chen, Y.A., Matsuura, Y., Mizuguchi, K.	Proteomic analysis of hepatitis C virus (HCV) core protein transfection and host regulator PA28γ knockout in HCV pathogenesis: a network-based study.	***J Proteome Res.***	11	3664-3679	2012
Fukuhara, T., Kambara, H., Shiokawa, M., Ono, C., Katoh, H., **Morita, E.**, Okuzaki, D., Maehara, Y., Koike, K., Matsuura, Y.	Expression of microRNA miR-122 facilitates an efficient replication in nonhepatic cells upon infection with hepatitis C virus.	***J Virol.***	86	7918-7933	2012
Morita, E., Yoshimori, T.	Membrane recruitment of LC3 proteins during autophagosome formation.	***Hepatol Res.***	42	435-441	2012
Morita, E.	ESCRT Differential requirements of mammalian ESCRTs in multivesicular body formation, virus budding and cell division.	***FEBS J.***	279	1399-1406	2012

Please cite this article in press as: Suzuki et al., Structural Basis of the Autophagy-Related LC3/Atg13 LIR Complex: Recognition and Interaction Mechanism, Structure (2014), http://dx.doi.org/10.1016/j.str.2013.09.023

Structure
Article

Structural Basis of the Autophagy-Related LC3/Atg13 LIR Complex: Recognition and Interaction Mechanism

Hironori Suzuki,[1,2,*] Keisuke Tabata,[3,4] Eiji Morita,[3] Masato Kawasaki,[2] Ryuichi Kato,[2] Renwick C.J. Dobson,[1,5,*] Tamotsu Yoshimori,[4,6] and Soichi Wakatsuki[2,7,8]

[1]Biomolecular Interaction Centre, School of Biological Sciences, University of Canterbury, Christchurch 8020, New Zealand
[2]Structural Biology Research Center, Photon Factory, Institute of Materials Structure Science, High Energy Accelerator Research Organization (KEK), Tsukuba, Ibaraki 305-0801, Japan
[3]International Research Center for Infectious Diseases, Research Institute for Microbial Diseases, Osaka University, Osaka 565-0871, Japan
[4]Department of Genetics, Graduate School of Medicine, Osaka University, Suita, Osaka 565-0871, Japan
[5]Department of Biochemistry and Molecular Biology, Bio21 Institute, University of Melbourne, Parkville, Victoria 3010, Australia
[6]Laboratory of Intracellular Membrane Dynamics, Graduate School of Frontier Biosciences, Osaka University, Suita, Osaka 565-0871, Japan
[7]Photon Science, SLAC National Accelerator Laboratory, Menlo Park, CA 94025-7015, USA
[8]Department of Structural Biology, School of Medicine, Stanford University, Stanford, CA 94305-5126, USA
*Correspondence: hironori.suzuki@canterbury.ac.nz (H.S.), renwick.dobson@canterbury.ac.nz (R.C.J.D.)
http://dx.doi.org/10.1016/j.str.2013.09.023

SUMMARY

Autophagy is a bulk degradation pathway that removes cytosolic materials to maintain cellular homeostasis. The autophagy-related gene 13 (Atg13) and microtubule associate protein 1 light chain 3 (LC3) proteins are required for autophagosome formation. We demonstrate that each of the human LC3 isoforms (LC3A, LC3B, and LC3C) interacts with Atg13 via the LC3 interacting region (LIR) of Atg13. Using X-ray crystallography, we solved the macromolecular structures of LC3A and LC3C, along with the complex structures of the LC3 isoforms with the Atg13 LIR. Together, our structural and binding analyses reveal that the side-chain of Lys49 of LC3 acts as a gatekeeper to regulate binding of the LIR. We verified this observation by mutation of Lys49 in LC3A, which significantly reduces LC3A positive puncta formation in cultured cells. Our results suggest that specific affinity of the LC3 isoforms to the Atg13 LIR is required for proper autophagosome formation.

INTRODUCTION

Autophagy is an essential intracellular process that maintains cellular homeostasis by degrading proteins, organelles, and bacterial pathogens. Dysfunction of the autophagy pathway causes a range of diseases in humans, including cancers, the neurodegenerative diseases such as Alzheimer's and Parkinson's, myopathies, and heart and liver diseases (Mizushima et al., 2008; Levine and Kroemer, 2008; Dikic et al., 2010). The process is widely conserved, from yeast to higher eukaryotes.

Autophagy has been particularity well characterized in yeast. Here, the process is initiated by the autophagy-related gene 1 complex (the Atg1 complex), which consists of Atg1 (Kamada et al., 2000), Atg13 (Funakoshi et al., 1997), Atg17 (Kamada et al., 2000), Atg29 (Kawamata et al., 2005) and Atg31 (Kabeya et al., 2007). Atg1 complex formation is regulated by target of rapamycin complex 1 (TORC1) and protein kinase A (PKA). Under stress-free conditions, the Atg1 complex is phosphorylated and inactivated by TORC1 and PKA. However, upon the induction of autophagy by intracellular signals (nutrient starvation or endoplasmic reticulum stress) or extracellular signals (invasion of pathogens), TORC1 and PKA are switched off, activating autophagy by allowing the Atg1 serine/threonine kinase to phosphorylate the Atg1 complex. The Atg1 complex is then recruited to double membrane structures, known as isolation membranes.

In human cells, Atg1 and Atg13 are conserved, although Atg1 is known as Unc-51-like kinase 1 (ULK1; Chan et al., 2007, 2009). The human homologs of Atg17, Atg29, and Atg31 are not reported; however, the focal adhesion kinase family interacting protein of 200 kDa (FIP200) is thought to play the role of Atg17 (Hara et al., 2008), and Atg101 has been identified as a component of the human Atg1 complex, called the ULK1 complex (Hosokawa et al., 2009). It was recently reported that Atg8 interacts with the Atg1 protein via the W/Y/FxxL/I/V motif (known as the LC3-interaction region [LIR]) promoting Atg1 degradation in the vacuole by recruiting the complex to the autophagosome (Kraft et al., 2012).

Atg8 is one of the autophagy-related genes that are indispensable for autophagosome formation, membrane tethering, and hemifusion (Nakatogawa et al., 2007). In yeast, only one Atg8 protein has been identified, whereas in human cells, seven Atg8 homolog proteins are reported and these are categorized into three subfamilies: microtubule associate protein 1 light chain 3 (which we call LC3A, LC3B, and LC3C in this work), γ-amino-butyric acid receptor-associated protein (GABARAP, GABARAPL-1, and GABARAPL-3), and golgi-associated adenosine triphosphatase enhancer of 16 kDa (GATE-16, also known as GABARAPL-2; He et al., 2003; Xin et al., 2001).

These Atg8 family proteins undergo multistep modifications: first by the cysteine protease Atg4, then the E1-like (ubiquitin

Please cite this article in press as: Suzuki et al., Structural Basis of the Autophagy-Related LC3/Atg13 LIR Complex: Recognition and Interaction Mechanism, Structure (2014), http://dx.doi.org/10.1016/j.str.2013.09.023

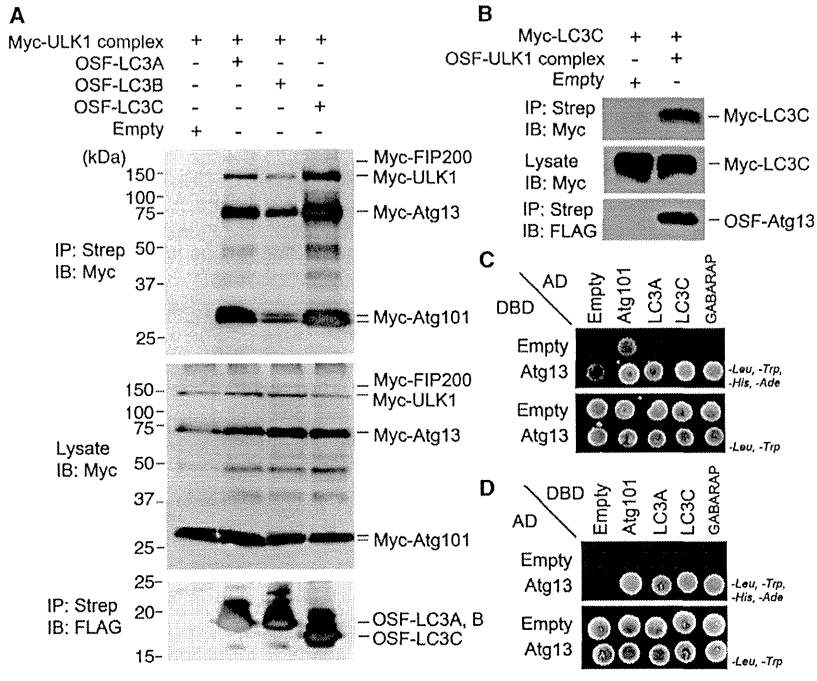

Figure 1. The ULK1 Complex Interacts with LC3 Family Proteins

(A) Myc-ULK1 complex (mixture of Myc-Atg13, Myc-Atg101, Myc-ULK1, and Myc-FIP200) coprecipitate with empty vector controls (lane 1), OSF-LC3A (lane 2), OSF-LC3B (lane 3), or OSF-LC3C (lane 4).

(B) ULK1 complexes coprecipitate with LC3C. Myc-LC3C coprecipitations with empty vector controls (lane 1), OSF-Atg13 (lane 2).

(C and D) Directed yeast two-hybrid interactions between human Atg13 and LC3 family proteins. The top array shows doubly transformed yeast replica plated on minus Leu, minus Trp, minus His, minus Ade selection media, where successful growth represents a positive protein interaction. The bottom array shows replica-plated yeast on minus Leu, minus Trp media (a control for equivalent transformation and yeast growth). The indicated constructs were fused to activating domains (ADs) or DNA binding domains (DBDs). Unfused DBD and AD constructs are shown as negative controls.

activating) enzyme Atg7, and finally the E2-like (ubiquitin conjugating) enzyme Atg3; as a result, they are conjugated to the autophagosome membrane in the following manner. In the first step, newly synthesized Atg8 family proteins are immediately cleaved at its C terminus by Atg4, resulting in the exposure of the C-terminal conserved glycine residue (Hemelaar et al., 2003; He et al., 2003; Tanida et al., 2004; Li et al., 2011). Atg7 forms a thioester intermediate with Atg8, followed by the conjugation of phosphatidylethanolamine by Atg3, which anchors the Atg8 family proteins to the autophagosome membrane (Schlumpberger et al., 1997; Tanida et al., 1999; Taherbhoy et al., 2011). In this process, Atg8 family proteins play a role not only in the elongation of the autophagosome membrane, but also in the recruitment of specific cytosolic materials to the autophagosome membrane, such as unfolded or aggregated proteins, mitochondria, and bacterial pathogens, via adaptor proteins that have the LIR motif. Hence, the process is called selective autophagy (Ichimura and Komatsu, 2010; Johansen and Lamark, 2011).

Five Atg8 structures in complex with LIRs have been reported: Atg8/Atg19 (Noda et al., 2008); LC3/Atg4B (Satoo et al., 2009); LC3B/p62 (Noda et al., 2008; Ichimura et al., 2008); LC3C/NDP52 (von Muhlinen et al., 2012); and GABARAP/neighbor of BRCA1 gene 1 (NBR1; Rozenknop et al., 2011). Despite these studies, the interaction mechanism remains unknown, although it has been demonstrated that the side-chains of Trp/Phe/Tyr and Leu/Ile/Val recognize two different hydrophobic surfaces on Atg8 proteins, named the W- and L-sites by Noda et al. (2010). Recently, Alemu et al. (2012) reported that Atg8 family proteins directly interact with ULK1, Atg13, and FIP200, members of the Atg1/ULK1 complex, through the LIR, and characterized ULK1 and Atg13 LIR motifs binding to GABARAP. The ULK1 LIR motif is required for starvation-induced autophagosome formation (Alemu et al., 2012).

In this article, we describe the binding interaction between Atg13 and LC3. Employing in vitro binding assays, we have independently determined that Atg13 directly interacts with LC3 via the LIR located at its C terminus. To probe the structural basis and mechanism of this interaction, we have used X-ray crystallography to solve the structures of LC3A and LC3C, along with the structures of LC3 isoforms in complex with a peptide containing the residues 436–447 of Atg13, which includes the LC3 interaction region W/Y/FxxL/I/V. Structural comparison reveals that binding of the LIR to LC3 induces a structural change of the side-chain of Lys49 of LC3, exposing a hydrophobic surface to accept the LIR. This movement is conserved in the LC3 family proteins. We verified the role of Lys49 by mutagenesis, which significantly reduces autophagosome formation. Together, our data demonstrate that Lys49 plays an important role in regulating the interaction with LIR-containing proteins in autophagy.

RESULTS

Atg13 Binds to LC3 Isoforms

The four known ULK1 complex subunits (ULK1, FIP200, Atg101, and Atg13), which included a One-STrEP-FLAG (OSF) tag, were simultaneously coexpressed in human embryonic kidney 293T cells (HEK293T) cells to create "baits" that could be used to identify ULK1 complex binding proteins. The resulting mixture of ULK1 complex proteins was affinity purified on a Strep-Tactin resin, which captured Atg13 and its binding partners. Bound proteins were separated by SDS-PAGE and identified by mass spectrometry analysis, which, remarkably, identified two different Atg8/LC3 family proteins as the ULK1 complex coprecipitates (LC3A and LC3C; data not shown). These interactions were initially verified by demonstrating that Myc-tagged ULK1 complexes bound to immobilized OSF-LC3A, OSF-LC3B, and OSF-LC3C, but not to control resins (Figure 1A). Reciprocal

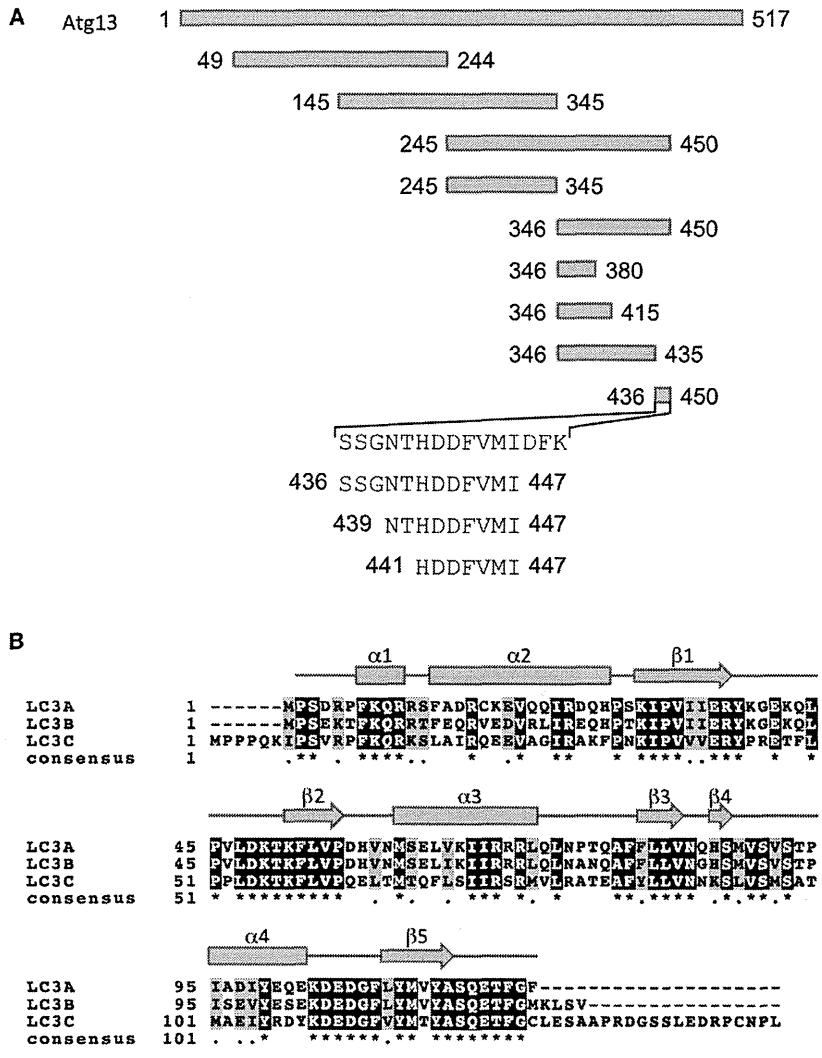

Figure 2. Schematic Representation of Atg13 and LC3 Isoforms

(A) The Atg13 deletion mutants and LIR peptides for the interaction analysis.

(B) Sequence alignment and secondary structure representation of LC3 isoforms. The multiple sequence alignment was generated by ClustalX2 (Larkin et al., 2007) using a box shade representation by BOXSHADE 3.21 (http://embnet.vital-it.ch/software/BOX_form.html). The bar shows the region of LC3A constructs that is used in this study (2–121) along with the secondary structures estimated using the DSSP program (Kabsch and Sander, 1983; boxes are α helices and arrows β strands).

interactions were also confirmed by testing that Myc-tagged LC3C bound specifically immobilized OSF-ULK1 complexes (Figure 1B). The LC3 family proteins also exhibited positive two-hybrid interactions with the Atg13 subunit, but not with the FIP200, ULK1, or Atg101 subunits (Figures 1C and 1D; data not shown). These results indicate that the Atg13 subunit of this complex is responsible for the interaction with the LC3 family proteins.

Mapping the LC3 Binding Region in Atg13

To determine the LC3 binding sites in Atg13, we performed glutathione S-transferase (GST) pulldown assays using a range of Atg13 truncated mutants and the three LC3 isoforms, LC3A, LC3B, and LC3C (Figure 2). Expressed proteins corresponding to the regions of 49–244, 145–345, and 245–450 of Atg13 were inserted into the pCold Trigger Factor (TF) vector and expressed in *E. coli* as 6xHis-TF fused proteins. The GST-LC3 proteins were bound to glutathione Sepharose 4B (GS4B) resin and mixed with 6xHis-TF-Atg13 constructs (Figure 3A). The 6xHis-Atg13$^{245–450}$ was pulled down with GST-LC3A and GST-LC3C, but not with GST-LC3B. For further investigation, we divided the region from 245 to 450 of Atg13 as shown in Figure 2A. These proteins were expressed in *E. coli* and immobilized on GS4B resin. GST-LC3s were cleaved by thrombin and separated using size exclusion chromatography. Purified LC3s were incubated with the resin immobilized with the GST-Atg13 constructs (Figures 3B–3D). All three LC3 isoforms bound to Atg13$^{346–450}$ and Atg13$^{436–450}$. Although initial binding experiments did not show binding between 6xHis-TF-Atg13 and GST-LC3B, further pulldown experiments using additional truncated LIR constructs demonstrated that 15 amino acids (436-SSGNTHDDFVMIDFK-450) is sufficient to be recognized by the three LC3 isoforms, whereas the mutants of Atg13 lacking residues 436–450 (346–380, 346–380, and 346–435) did not bind to LC3s. The LC3 binding region of Atg13 identified here includes a motif similar to the LIR reported previously, xxxW/YxxL/I/V, where x is an acidic residue (Noda et al., 2008; Ichimura et al., 2008; Noda et al., 2010; Atg13, 441-HDDFVMI-447) and corresponds to the region reported by Alemu et al. (2012). This investigation demonstrated that LC3 isoforms bind to Atg13 via the LIR motif.

Dissociation Constants for the LC3 Interaction with LIR

To characterize the interaction kinetics between the Atg13 LIR variants and LC3s, we performed real-time interaction analysis using a surface plasmon resonance (SPR) biosensor, three GST-tagged constructs of the Atg13 LIR (436–447, 439–447 and 441–447), and the LC3A, LC3B, and LC3C isoforms. A range of concentrations of each LC3 isoform were injected onto the GST-Atg13 LIR peptides immobilized to a sensor chip via an anti-GST antibody. All three LC3 proteins demonstrated concentration-dependent increases in resonance signals (Figure S1 available online). The apparent dissociation constants (K_D) for the Atg13 LIR peptide/LC3s interaction were calculated using

Please cite this article in press as: Suzuki et al., Structural Basis of the Autophagy-Related LC3/Atg13 LIR Complex: Recognition and Interaction Mechanism, Structure (2014), http://dx.doi.org/10.1016/j.str.2013.09.023

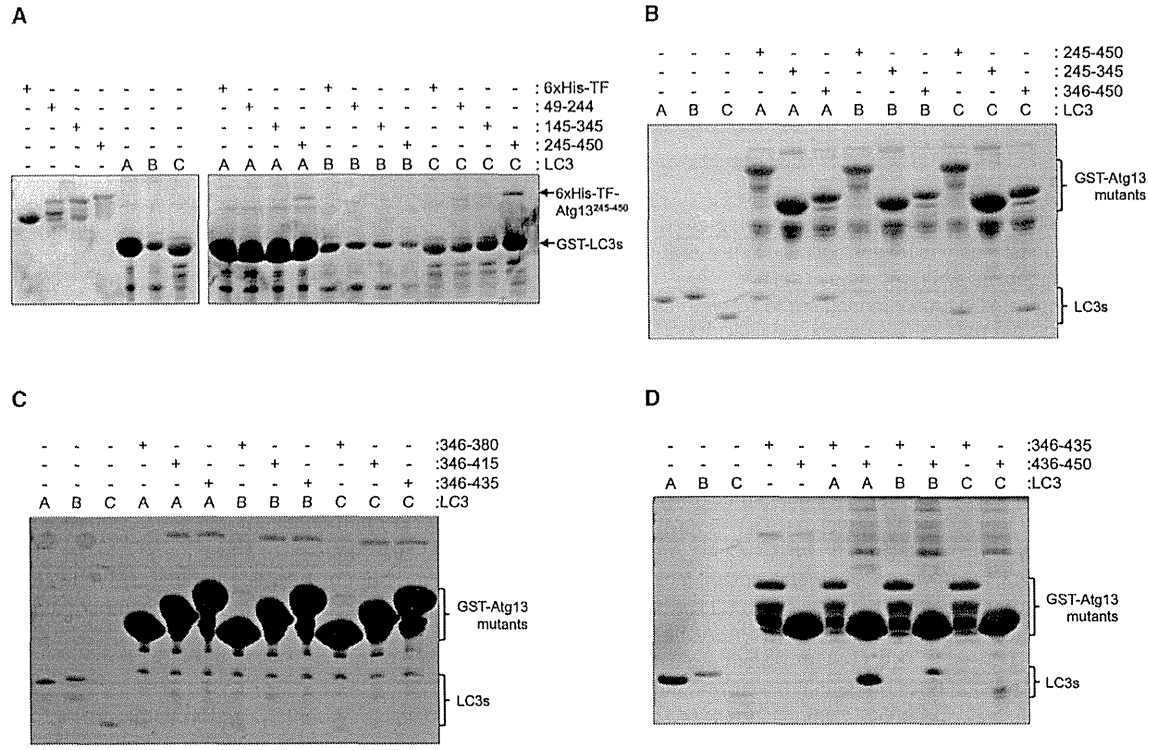

Figure 3. Identification of Atg13 LIR by Pulldown Assay

GST pulldown assays were performed using GST-LC3 isoforms and 6xHis-TF-Atg13 (A) or GST-Atg13 and LC3 isoforms (B–D). GST-fusion proteins were immobilized on Glutathione sepharose 4B and mixed with purified counterpart proteins. Pulldown products were subjected to SDS-PAGE and detected by Coomassie brilliant blue (CBB) staining.

the Scatchard plot analysis (resonance unit versus resonance unit/concentration [RU versus RU/concentration]). The K_D values for LC3A were 17.5 ± 0.2 μM (GST-Atg13$^{436–447}$), 16.4 ± 0.3 μM (GST-Atg13$^{439–447}$), and 18.3 ± 0.6 μM (GST-Atg13$^{441–447}$); those for LC3B were 57 ± 4 μM, 50 ± 3 μM, and 52 ± 7 μM, respectively; and those for LC3C were 12 ± 4 μM, 10 ± 3 μM, and 13 ± 6 μM (n = 3), respectively. Clearly, the addition of the N-terminal residues to the Atg13 LIR did not affect the binding affinities. The overall amino acid sequence identity between LC3A and LC3B is 83%, whereas between LC3A and LC3C, or LC3B and LC3C, it is only 55%. However, the binding affinity of LC3B to the Atg13 LIR is appreciably lower than that of LC3A or LC3C to Atg13 LIR. These data demonstrate that the region of Atg13 from 441 to 447 is sufficient to interact with LC3s and that LC3B may have a different LIR binding mode, given the lower affinity compared with LC3A and LC3C.

Structures of Uncomplexed Three LC3 Isoforms and the Isoforms in Complex with the Atg13 LIR

To elucidate the structural basis of the interaction between Atg13 and LC3s, we used X-ray crystallographic analysis to solve the structures of LC3A (2.00 Å; Protein Data Bank [PDB] code 3WAL) and LC3C (1.75 Å; PDB code 3WAM). In addition, we solved the complex forms of all three isoforms using chimeric proteins of Atg13$^{436–447}$-LC3A (1.77 Å; PDB code 3WAN), Atg13$^{436–447}$-LC3B (2.60 Å; PDB code 3WAO), and Atg13$^{436–447}$-LC3C (3.10 Å; PDB code 3WAP), and recently we reported a high-resolution structure of LC3B (1.60 Å; PDB code 3VTU; Rogov et al., 2013). Data collection and refinement statistics are summarized in Table 1 and the overall structures are depicted in Figure 4. Overall structures of the uncomplexed LC3 isoforms are closely aligned (RMSD values: LC3A versus LC3B = 0.7 Å, LC3A versus LC3C = 1.2 Å, LC3B versus LC3C = 1.3 Å), with noticeable differences in the loops between α3 and β4 and the region including β4, β5, and α4 (Figure 4). The asymmetric unit of the Atg13-LC3A contains two molecules, whereas the crystal structure of Atg13-LC3C contains only one and that of Atg13-LC3B contains four molecules, in which molecules A and B bind to molecules D and C, respectively (Figure S2). Interestingly, each of the chimeric molecules are packed within the crystal such that the Atg13$^{436–447}$ N-terminal region interacts, not with its fused LC3 domain, but with an LC3 domain related by the crystallographic symmetry (Atg13-LC3A, Atg13-LC3B, and Atg13-LC3C) and a noncrystallographic symmetry (Atg13-LC3B).

A comparison of the uncomplexed LC3 isoform structures to the Atg13-LC3 chimeric structures shows that the overall topologies are very similar. The electron density for the N terminus of the Atg13 LIR was not visible for Atg13-LC3A and Atg13-LC3B (residues Ser436 to His441) or for Atg13-LC3C (residues Ser436 to Glu443; Figure S3). This implies that the N terminus of the Atg13 LIR is not involved in the interaction, which is consistent with our detailed interaction experiments presented above

Table 1. Data Collection and Refinement Statistics

	LC3A	LC3C	Atg13$^{436-447}$-LC3A	Atg13$^{436-447}$-LC3B	Atg13$^{436-447}$-LC3C
PDB code	3WAL	3WAM	3WAN	3WAO	3WAP
Region of LC3	2–121	8–125	2–121	2–119	8–125
Data Collection					
Beamline	PF BL-17A	PF BL-5A	PF BL-17A	PF BL-17A	PF BL-17A
Wavelength (Å)	0.9800	1.0000	0.9800	0.9800	0.9800
Space group	$I4_1$	$P3_121$	$P2_1$	$P4_1$	$P3_121$
a, b, c (Å)	93.0, 93.0, 33.1	71.7, 71.7, 55.7	37.7, 47.9, 77.1	64.6, 64.6, 130.3	61.7, 61.7, 95.9
α, β, γ (°)	90.0, 90.0, 90.0	90.0, 90.0, 120.0	90.0, 94.2, 90.0	90.0, 90.0, 90.0	90.0, 90.0, 120.0
Resolution (Å)	46.5–2.00 (2.11–2.00)	27.8–1.75 (1.84–1.75)	47.9–1.77 (1.87–1.77)	43.4–2.60 (2.74–2.60)	53.5–3.10 (3.27–3.10)
Number of measured reflections	68,775 (10,192)	178,722 (25,835)	86,532 (11,807)	62,527 (8,938)	39,951 (6,084)
Number of unique reflections	9,793 (1,422)	16,985 (2,430)	24,414 (3,447)	16,435 (2,372)	4,045 (588)
Completeness (%)	100.0 (100.0)	99.8 (100.0)	99.0 (96.7)	99.9 (99.5)	98.5 (100.0)
R_{merge} (%)	7.4 (38.2)	9.3 (36.6)	5.9 (19.4)	6.8 (74.0)	6.9 (78.5)
I/σI	18.2 (5.1)	16.2 (6.3)	12.6 (4.9)	14.4 (2.4)	15.7 (2.8)
Refinement					
R_{work}/R_{free} (%)	18.1/23.7	17.2/23.7	17.4/22.7	22.3/29.4	21.0/26.6
Mean B value (Å^2)	35.1	23.7	18.7	61.5	144.7
Rmsd bond length (Å)	0.019	0.034	0.022	0.011	0.014
Rmsd bond angle (°)	1.943	2.446	2.145	1.801	2.445
Ramachandran plot					
Favored/allowed/outlier (%)	100/0/0	98.2/1.8/0	98.8/1.2/0	98.2/1.8/0	99.2/0.8/0
Number of molecules in the asymmetric unit	1	1	2	4	1

Highest resolution shell is shown in parentheses. rmsd, root-mean-square deviation.

in which truncated peptides 436–447, 439–447, and 441–447 bind to LC3s equally well. The Atg13 LIR in all three chimeric proteins were recognized by the same hydrophobic pockets of LC3, consisting of side-chains of Ile23, Lys49, Lys51, Phe52, Leu53, Ile66, and Phe108 via hydrophobic interactions to Phe444 of the Atg13 LIR (the W-site) and by main-chain hydrogen bonding between Lys51 and Leu53 of LC3 and Val445 and Ile446 of the Atg13 LIR (the L-site; Tables S1 and S2). A comparison with the binding interactions found in the previously reported crystal structure of the LC3B/p62 complex (Ichimura et al., 2008; PDB code 2ZJD) shows that the W/Y/FxxL/I/V motif, which in Atg13 is 444-FVMI-447 and in p62 is 340-WTHL-343, holds a similar conformation with similar interactions.

Lys49 Undergoes a Large Structural Rearrangement upon Atg13 LIR Binding

We then investigated side-chain structural arrangements by comparing the LC3A and Atg13-LC3A structures with sufficiently high resolutions, 2.00 Å and 1.77 Å, respectively. In the Atg13-LC3 isoform complex structures, the side-chains of Ile23, Lys49, Lys51, Phe52, Leu53, Ile66, and Phe108, and additionally in the Atg13-LC3A complex structure Glu19, His27, Lys30, and Pro55 of LC3, are involved in the interaction with Atg13$^{436-447}$ (Figure 5A). Upon Atg13$^{436-447}$ binding, these residues, except for Lys49, move slightly to reorganize (Figures 5A and 5B). In contrast, the side-chain of Lys49 in LC3A undergoes a large rotamer rearrangement. According to Wild et al. (2011), the Lys49 movement upon the optineurin LIR binding was also observed by the nuclear magnetic resonance experiment. In the uncomplexed structure, the gamma and epsilon carbon atoms of Lys49 form hydrophobic interactions with the aromatic ring of Phe52 (Figure 5C). However, in the complexed structure, the side-chain of Lys49 shifts by as much as 6.7 Å at the zeta nitrogen to open the hydrophobic interaction surface; as a result, both Phe52 and Lys49 form hydrophobic interactions with Val445 of Atg13 LIR.

Critical Residues for the Binding of Atg13 with LC3A

To determine the contribution of individual amino acid residues of Atg13 to the interaction with LC3, we measured relative binding abilities of point mutations in Atg13 compared with the wild-type (WT) protein using an SPR biosensor. The GST-fused Ala-substituted Atg13 LIR peptides were immobilized onto an SPR sensor chip via anti-GST antibodies (Figure 6A), and LC3A was injected onto the sensor chip. As shown in Figure 6B, the binding affinity to LC3A of all Ala-substituted mutants decreased significantly. In particular, the mutations of Phe444 (M4) and Ile447 (M7) to Ala reduced the binding affinity to ~25% (Figure 6B). The control protein (GST-GS) did not bind to LC3A.

Next, we investigated which residues in LC3A are required for Atg13 binding. In this experiment, we prepared six single mutations of LC3A to probe the LIR binding (Figure 6C). The first was